Solid solution strengthening and deformation behavior of single-phase Cu-base alloys under tribological load

Stephan Laube[a], Alexander Kauffmann[a], Friederike Ruebeling[a,b], Jens Freudenberger[c,d], Martin Heilmaier[a] and Christian Greiner[a,b] *

[a] Karlsruhe Institute of Technology (KIT), Institute for Applied Materials (IAM), Kaiserstrasse 12, 76131 Karlsruhe, Germany

[b] KIT IAM-CMS MicroTribology Centrum µTC, Strasse am Forum 5, 76131 Karlsruhe, Germany

[c] Leibniz IFW Dresden, Helmholtzstraße 20, 01069 Dresden, Germany

[d] TU Bergakademie Freiberg, Institute of Materials Science, Gustav-Zeuner-Str. 5, 09599 Freiberg, Germany

* corresponding author; mail: christian.greiner@kit.edu (C. Greiner)

Abstract (239 / 250 words)

The influence of solid solution strengthening on the evolution of the microstructure under cyclic dry sliding is still not fully rationalized. One reason is that alloying needed for solid solution strengthening alters the stacking fault energy at the same time and, hence, the mode of dislocation slip in face-centered cubic metals and alloys. Both aspects determine the details of plastic deformation and, therefore, lead to different results under tribological load. A series of Cu-Mn alloys was investigated in the present investigation, which exhibit wavy slip mode and an almost constant stacking fault energy over a wide solute concentration range. Solid solution strengthening is the main contribution to the hardness in these alloys. The sole impact of changing strength and hardness on the tribological response along with microstructure evolution during tribological load is assessed. After the reciprocating, tribological loading a linear correlation between the wear track width and hardness could be ascertained. Electron microscopy reveals a horizontal discontinuity of the dislocation structure beneath the surface in all alloys at a similar depth. An evaluation of the Hamiltonian elastic stress field model indicates that the depth of the dislocation feature after one sliding pass correlates with the stress distribution as well as the critical stress for dislocation motion. The subsurface microstructure features a transition from the dislocation feature to subgrain formation after about five to ten

cycles. Beyond ten cycles, oxide clusters are formed on the sliding surface and the grains elongate in the sliding direction.

Graphical abstract

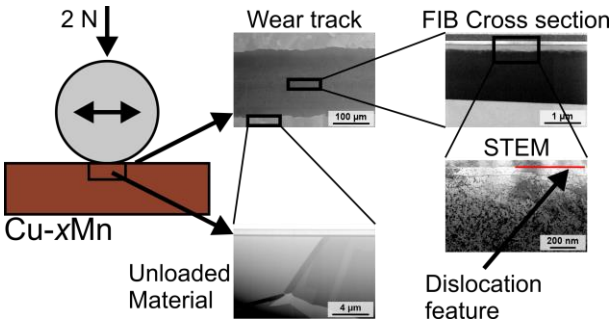

Keywords (4 / 6)

tribology; friction; copper-manganese alloys; solid solution strengthening

1. Introduction

While many processes in tribological contacts can be phenomenological described by simulations, the currently available microscopic models however prove to be inaccurate. One reason for this is the large number of intrinsic and extrinsic parameters that influence the friction and wear behavior of materials in contact [1,2]. Due to its industrial relevance, many publications have dealt with the wear behavior of metals and alloys, in particular those of commercial interest, at high loads and high relative speeds [3–6]. The focus was often placed on the description and characterization of the wear track and the mechanisms that occur as a result of material pairing and test parameters, like contact pressure and sliding speed [4–7]. To characterize a tribological system, the coefficient of friction is an important parameter because it is almost proportional to the energy dissipation during sliding [8]. Early research showed that the coefficient of friction is related to the plastic deformation of the near-surface region, which in particular can be described in terms of work hardening, recovery and microstructure [8–11]. Depending on the materials and environmental conditions, the plastic deformation leads to distinct observations, like dynamic recrystallization [12] and tribo-oxidation [12,13]. It was shown that nanocrystalline alloys tend to coarsen [14,15], while coarse grained metals and alloys undergo microstructural refinement under tribological load [16–20]. Argibay et al. [21] have argued that this is a result of the correlation between the microscopic deformation mechanisms (which are related to the existing microstructure) and the friction regime.

Wert et al. [22–24] revealed that a change in stacking fault energy (SFE) in Cu-based alloys significantly alters the wear behavior of the tribological system. However, to the best of our

knowledge, there is still no universal and quantitative approach available for accurately describe the impact of SFE on the tribological behavior. For example, studies by Blau [25] as well as Suh & Saka [26] revealed that there is no simple one-to-one correlation of the SFE and the formation of wear particles. Due to the complex nature of the dislocation-solute interactions, many material parameters such as, e.g. strength and hardness typically change along alloying. The appearance of slip in face-centered cubic (FCC) metals and alloys is significantly different depending on the value of the SFE: (i) 'High' SFE materials exhibit wavy slip, which changes to (ii) planar slip in 'medium to low' SFE materials. Finally, (iii) twinning-induced plasticity is additionally observed at sufficiently 'low' SFE [27]. The SFE is often used as an indicator to evaluate or even predict the active deformation mechanism and in particular the slip mode [28]. However, this evaluation fails, when the sample is not single-phase or a random solid solution anymore. For example, ordering phenomena like short-range order are known to have a more significant influence than the SFE on the slip mode, as indicated by Gerold and Karnthaler [29] as well as Wolf et al. [30]. Additionally, Hong and Laird [31] discussed the influence of the atomic size misfit parameter due to solutes on the slip mode. In detail, the active slip mode in alloys depends on the SFE, the shear modulus and the dislocation-solute interaction. As these are no independent measures, they proposed a weighted combination thereof to be responsible to the active slip mode and in particular for its gradual change. Recently, the model was extended by Hong [32] to predict twinning-induced plasticity in Cu alloys. In contrast to this, Wang [28] proposed that a change in the slope of the SFE as a function of the valence electron ratio (e/a) determines the change in the slip mode. In the high slope regime (low e/a, high to medium SFE) wavy slip is observed whereas a small slope results in planar slip. In many binary Cu-based alloys, the SFE declines significantly with increasing solute concentration as shown in Fig. 1.

This paper presents results on single-phase Cu-Mn solid solutions, which were investigated under mild tribological load. The objective of the investigation is to clarify the influence of solid solution strengthening on the evolution of the microstructure under cyclic dry sliding against a sapphire sphere. Cu-Mn was chosen as a model system because its SFE stays almost constant until about 12 at% Mn [33,34] as depicted in Fig. 1. Therefore, the e/a – SFE diagram (independent of the multi-valence nature of Mn) exhibits no significant change in slope. Independent of which quantity (neither SFE, e/a, nor the slope of the SFE-e/a-dependence) is considered to be responsible for changing the slip mode. Therefore changes in slip mode are not expected for the investigated Cu-Mn alloys. Hence, the sole impact of changing strength

and hardness on the tribological response and microstructure evolution during tribological load can be assessed.

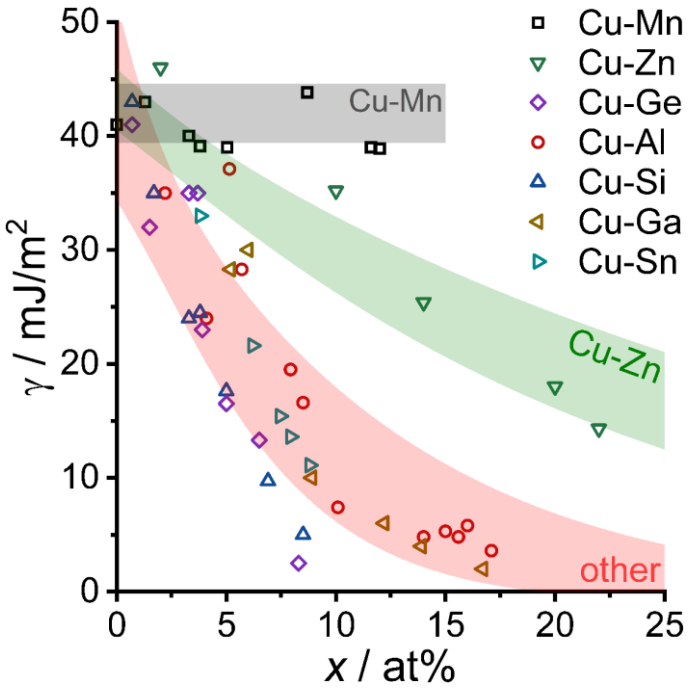

Fig. 1: SFE **γ** for different Cu alloys as a function of solute concentration. Literature references for the different alloys are Refs. [33,34] for Cu-Mn, Refs. [35], [36] for Cu-Ge and Cu-Si, Refs. [36], [37] for Cu-Al and Cu-Zn, Ref. [35] for Cu-Ga and Cu-Sn, respectively. An SFE of about 45 mJ/m² for Cu is assumed based on Refs. [34,35]. *x* denotes the molar fraction of solutes in Cu.

2. Experimental and materials

Alloy ingots were prepared by arc melting mixtures of pure, bulk elements. Cu and Mn with purities of 99.99 % were provided by chemPUR GmbH (Germany). Mn was etched with nitric acid (1:10 diluted with distilled water) before the melting process in order to remove the oxide layer. The elements were melted in a high purity Ar atmosphere using an AM/0.5 arc melting furnace by Edmund Bühler GmbH (Germany). The furnace chamber was evacuated and flushed with Ar for three times followed by pumping to high vacuum of $1 \cdot 10^{-4}$ mbar. After achieving high vacuum, a final Ar pressure for the melting process of 600 mbar was established. Prior to each melting step, a Zr lump was re-melted in order to remove residual oxygen in the atmosphere. Every button was flipped and re-melted at least five times to ensure homogeneity before casting into a water-cooled, cuboid-shaped Cu mold (15 x 20 x 50) mm. The alloys were homogenized in evacuated fused-silica tubes at 820 °C for 24 h and subsequently quenched in water. The homogenized alloys were unidirectional rolled at room temperature from $t_0 =$ 15 mm down to $t_f = 5$ mm in thickness (corresponding to a logarithmic degree of deformation $\varphi = \ln(t_0/t_f) = 1.1$). Samples for tribological testing with dimensions of (24 x 12 x 5) mm³

were cut via electrical discharge machining. Depending on the composition, the temperatures for the recrystallization treatment were chosen between 500 and 735 °C to achieve a similar grain size of about 30 µm. The heat treatments were conducted in evacuated fused-silica tubes inside an L3/S27 resistance furnace by Nabertherm (Germany) for 30 min followed by quenching in water. The composition of the as-cast alloy CuMn2 was determined by inductively coupled plasma-optical emission spectrometry (ICP-OES). Crystal structure was determined by X-ray diffraction (XRD) performed on a D2 Phaser system by Bruker (Germany) equipped with a LynxEye line detector and a Cu Kα radiation source. 2Θ ranges from 10° to 145° with a step width of 0.01° at an acquisition time of 384 s per step. The lattice parameter was determined by an extrapolation towards $\Theta = 90°$ using the weighting function $w(\Theta) = 1/2 \cdot (\cot^2\Theta + \cot\Theta \cdot \cos\Theta)$ according to Nelson-Riley [38]. All determined parameters of the investigated alloys are summarized in Table 1.

alloy	Mn content / at%	grain size / µm	lattice parameter / Å	microhardness HV0.1
Cu	-	50 – 100	3.6150	39.4 ± 1.3
CuMn2	2.1*	30.1 ± 1.2	3.6232	53.8 ± 0.9
CuMn4	4.1	29.3 ± 0.9	3.6316	61.3 ± 0.9
CuMn8	8.0	26.6 ± 0.9	3.6472	74.3 ± 1.7
CuMn12	12.0	26.3 ± 0.6	3.6625	82.9 ± 1.4

Table 1: Determined chemical composition in at% of the samples using standard-related energy dispersive X-ray spectroscopy (EDS) or ICP-OES (indicated by *). Additionally, grain size, lattice parameter and microhardness is given. The microhardness of Cu (99.99 % purity) was analyzed on a coarse grained and recrystallized sample. The lattice parameter of Cu was determined on a high purity, polycrystalline powder reference sample.

Prior to tribological testing, the sample surfaces were prepared by a standard metallographic procedure. After grinding to achieve co-planar surfaces, manual mechanical polishing was performed. The alloys were polished with 3 µm MetaDi Supreme followed by chemo-mechanical polishing with a non-crystallizing amorphous colloidal silica suspension (both supplied by Buehler, Germany) for about 10 min. The manual preparation was followed by a vibratory polishing step for 16 h. After the polishing steps, the samples were etched for 30 to 120 s using ammonium persulfate ($(NH_4)_2S_2O_8$) 1:10 diluted with distilled water. Afterwards, the samples were electro-polished for 15 s (CuMn2, CuMn4) or 60 s (CuMn8, CuMn12) in D2 electrolyte from Struers at a voltage of 6 V (CuMn2, CuMn4), 9 V (CuMn8) or 16 V (CuMn12) depending on the solute concentration. The samples were stored in a vacuum desiccator in order to minimize the natural oxidation of the surface. Right before tribological testing, the samples were sonicated in isopropanol for 15 min. These preparation steps ensured a subsurface microstructure with the least initial defect density possible (as verified by electron channeling

contrast from the surface and milled cross sections by focused ion beam (FIB) as depicted in Fig. 2 a & b for example). Microhardness was evaluated utilizing a Q10A+ Vickers hardness tester from Qness (Austria) by applying a load of 0.98 N (HV0.1). The average microhardness was determined from sixteen individual indentations on each sample. A reciprocating, linear tribometer setup was used for the sliding tests without lubrication. A fresh monocrystalline sapphire sphere (Al_2O_3), 10 mm in diameter, purchased from Saphirwerk AG (Switzerland) was utilized as a counter body for each cycle number. The total cycle number was systematically varied as 0.5 (single forward pass), 1 (single forward and reciprocal pass), 10, 100, 500 and 1000 cycles, respectively. All other obvious, macroscopic parameters were kept constant throughout the experiments. The relative humidity and temperature were at (50 ± 5) % and (22 ± 1) °C, respectively, during all experiments. The stroke length was 12 mm and the sliding speed was 0.5 mm/s. Further details regarding the tribological setup are described elsewhere [39]. The applied normal load was 2 N, which results in an estimated Hertzian pressure of about (560 – 570) MPa for a standing contact with no contact deformation. For the calculation, Young's modulus and Poisson ratios determined from ultrasonic phase spectroscopy measurements were utilized for the Cu alloys. Ultrasonic phase spectroscopy is described elsewhere [40]. Information about the sapphire was taken from the data sheet provided by Saphirwerk AG. The determined Young's moduli are (126 ± 0.5) GPa and (123.8 ± 0.1) GPa for CuMn(2 – 8) and CuMn12, respectively. The shear moduli ascertained by this method remain constant at 47 GPa at an uncertainty of about 1 GPa. The wear tracks and the microstructure were investigated by means of scanning electron dual beam microscopy (SEM) using a Helios NanoLab™ 650 from FEI (Oregon, USA) and its secondary electron (SE) and back-scattered electron (BSE) detectors. Energy dispersive X-ray spectroscopy (EDS) was performed using an X-Max detector by Oxford Instruments (England). The deformed surface layers were characterized by SEM images of cross sections parallel to the sliding direction, perpendicular to the surface and in the center of the wear scar. For the preparation of the transmission electron microscopy (TEM) foils a state of the art FIB lift-out technique was applied [41]. To protect the worn surface of the cross sections as well as the TEM foils from the Ga^+ ion beam damage, two Pt layers were applied by either electron or ion beam deposition, respectively. Scanning transmission electron microscopy (STEM) was conducted with an acceleration voltage of 30 kV and a beam current of 100 pA inside the Helios NanoLab™ 650. The average width of the wear tracks was determined from at least 15 different positions. Grain size was obtained by intercept method on three randomly placed BSE micrographs for each alloy. The mean surface roughness (S_a) of all samples was below 128 nm. At least three areas

of (1.275 x 0.956) mm² were scanned using a PLu neox optical profiler from Sensofar-Tech, SL (Spain) equipped with a phase shift interferometric objective lens (DI10X-N). Wear of the monocrystalline sapphire counter body was not detected in this investigation.

3. Results and discussion

3.1. Material characterization

For the tribological tests, the surface has to be (almost) free of deformation in order to obtain reliable results. The surface of CuMn2 is depicted in Fig. 2a using BSE imaging with electron channeling contrast as an example demonstrating the material processing and sample preparation quality. Deformation cannot be detected on the sample surfaces which would lead to varying contrast within the individual grains. This was supported by preparing cross sections into the surface by FIB. A corresponding SE micrograph of the cross section is shown in Fig. 2b, where surface-near contrast changes cannot be obtained within the different grains. Hence, the surfaces before tribological testing can be considered to be free of deformation.

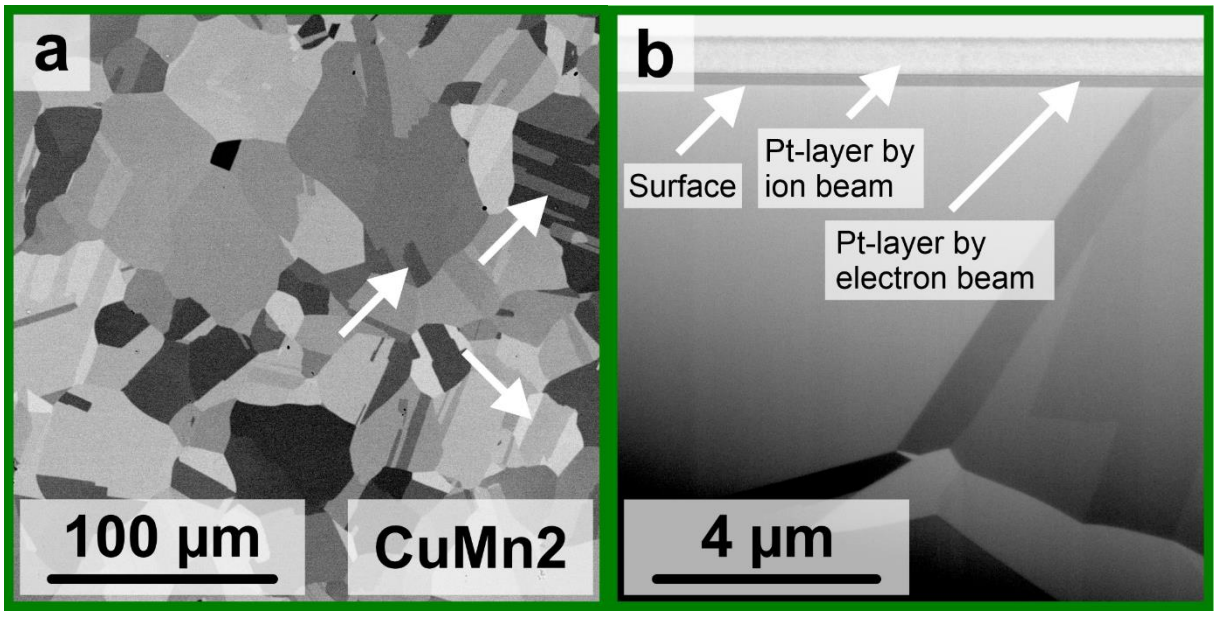

Fig. 2: SEM micrographs of CuMn2; (a) BSE contrast image revealing a grain size of about 30 µm, some twin boundaries are indicated by white arrows. (b) Micrograph using SE contrast imaging of a FIB-prepared cross section of the sample shown in (a).

FCC single-phase microstructure was additionally confirmed by XRD measurements for all samples (the corresponding diffraction pattern are displayed in Fig. S1). The determined lattice parameters and microhardness values are depicted in Fig. 3 and summarized in Table 1. A good agreement with literature data [42,43] is observed for the lattice parameters. It follows an almost linear trend with $(3.615(0) + 0.400(2)\ x)$ Å, where x denotes the molar fraction of Mn. As

presented in Fig. 3, the microhardness of the investigated alloys increases monotonically with the solute content due to the active strengthening mechanism in these alloys.

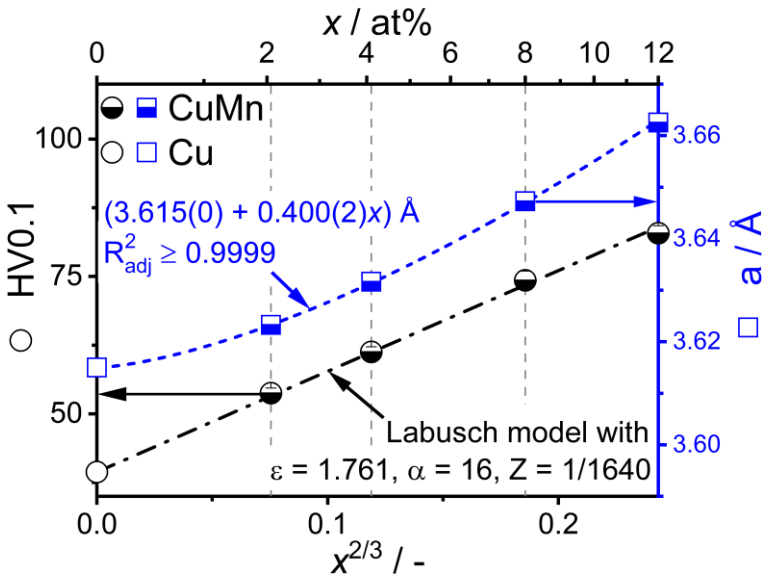

Fig. 3: Microhardness HV0.1 and lattice parameters **a** of the recrystallized samples as function of solute concentration *x*. The blue dotted line is a linear approximation of the lattice parameter according to Vegard's law [44]. The modeled hardness based on the Labusch model for solid strengthening is depicted by the black dash-dot line (please see text and Eq. (1) for details). The values for pure Cu are presented in Table 1.

Since the present alloys are single-phase without any secondary phases, only solid solution strengthening has to be considered as major strengthening contribution. All samples were in the fully recrystallized condition and they exhibit a similar grain size, i.e. 26 to 30 µm (see Table 1). Therefore, dislocation strengthening can be neglected and grain boundary strengthening is supposed to contribute to the total strength in all alloys at a comparable level.

According to the Labusch model for solid solution strengthening [45], the increase in yield strength is described by accounting for the dielastic $\eta = \frac{1}{G}\frac{\mathrm{d}G}{\mathrm{d}x}$ and parelastic $\delta = \frac{1}{a}\frac{\mathrm{d}a}{\mathrm{d}x}$ contributions. G and a are the shear moduli and lattice parameters of the alloys, respectively. The maximum obstacle force depends on $\epsilon = (\eta' + \alpha^2\delta^2)^{1/2}$ (with $\eta' = \frac{\eta}{1+|\eta|/2}$) and, finally, the relationship between the increase in yield strength $\Delta\sigma_{SS}$ and solute concentration x is as given in Eq. (1):

$$\Delta\sigma_{SS} = 3\,Z\,G\,\epsilon^{4/3}\,x^{2/3} \qquad (1)$$

The corresponding η' and δ, which were obtained from literature and the experimental lattice parameters (provided in Table 1), are summarized in Table 2, respectively. The parameter α accounts for differences in the interaction forces depending on the dislocation character and the type of solute. For single-phase Cu alloys, α typically yields values in the order of 16 [45]. For the present investigation, Z acts as a fitting parameter and incorporates the following aspects,

which are unknown or considered similar among the alloy series: (i) The calculated yield strengths are converted to Vickers hardness values which correspond to the respective yield strengths under simple compression at a plastic strain of approximately 0.08 [46]; (ii) Z incorporates the temperature-dependent yield strength of the Cu-Mn alloys, because in the strict sense the Labusch model only describes the dislocation-solute interactions at 0 K.

Ref.	δ	η'	ϵ
this paper	0.107	-0.414†	1.761
[30]	0.103	-0.406	1.697 (2.054‡)
[47]	0.11	-	-

Table 2: Modeling parameters for solid solution strengthening of Mn in Cu. $\boldsymbol{\delta}$ is obtained from the experimental lattice parameter presented in Table 1. $\boldsymbol{\eta'}$ is calculated on the basis of precisely determined shear moduli in Ref. [34]. For comparison, literature data from Refs. [30] & [47] are shown as well. Note that $\boldsymbol{\epsilon}$ was originally calculated by using $\boldsymbol{\epsilon = |\eta' - \alpha\delta|}$ in Ref. [30] (highlighted by ‡). For the sake of comparability, this quantity was re-calculated using the more frequently used equation, which is also used throughout this article.

As presented in Fig. 3, the determined increase in microhardness can be well described by the Labusch model for solid solution strengthening. This is anticipated from literature [30,47] as well as some minor deviations from the ideal relationship at high solute concentrations. Beyond a solute concentration of about 1 at% Mn, Cu-Mn alloys can exhibit some degree of local order or clustering [42,48] which can alter the solid solution strengthening contributions. However, heat treatments of Cu-Mn alloys which lead to some kind of ordering phenomena typically last significantly longer and are conducted at lower temperatures. For example 450 °C for 95 h as mentioned in Ref. [42] (based on data taken from Ref. [49]) than the applied recrystallization treatment from the present investigation (650 to 725 °C for 30 min).

3.2. Friction behavior and worn surfaces

In order to allow comparability to other studies, the tribological characteristics are briefly summarized. These tribological properties are however not the scope of the present article, which is the influence of the solid solution strengthening on subsurface microstructural evolution. The determined steady state coefficients of friction (COF) are in the range of 0.5 to 0.7 (see Fig. S2). The observed running-in behavior is in accordance with literature for oxidizing metals and alloys in ambient atmosphere [13,50] Formation of wear particles was detected after 100 cycles; the size and shape of the wear particles depend on the solute concentration. In the early stages, adhesion is the prominent wear mechanism and shifts to abrasion and surface oxidation for higher cycle numbers. Additionally, the detected wear particles are larger (around 1 – 10 µm) and the quantity increases with the Mn concentrations (see Fig. S3 for wear at the dead ends of the wear track).

3.3. Tribological induced surface deformation

To quantitatively analyze the influence of the hardness on the plowing resistance, the track width, as highlighted by a white arrow in Fig. 4a, is considered as a quantitative measure for wear in the following. The concept of wear used in the upcoming section is related to surface deformation and not in particular on loose particle formation and oxidation due to tribological loading. In Fig. 4b, the determined track widths are depicted as a function of the hardness from one up to 100 cycles. Beyond 100 cycles, a pronounced level of surface oxidation was observed [13]. Additionally, the severe plastic deformation of the surface from each cycle influences all subsequent cycles with additional work hardening of the surface. The presented results support the postulation [25,26] that the SFE cannot be taken as a clear indicator of the wear behavior of alloys, in particular at higher cycle counts (100 and more cycles). Therefore, these high cycle numbers will not be discussed any further. The track width exhibits a linear correlation with the microhardness of the alloys in the unloaded state with $R^2_{adj} > 0.93$. This result is rationalized by the classical abrasive wear theory [51,52], which yields a wear rate inversely proportional to the bulk hardness. This is noteworthy, because the surface hardness within the wear track is known to change significantly due to the tribologically induced strain near the surface [10,53]. In case of the strengthening from grain size reduction and dislocations, it could be shown that the wear resistance increases significantly in comparison with the coarse-grained metals or alloys (e.g. see Ref. [50]).

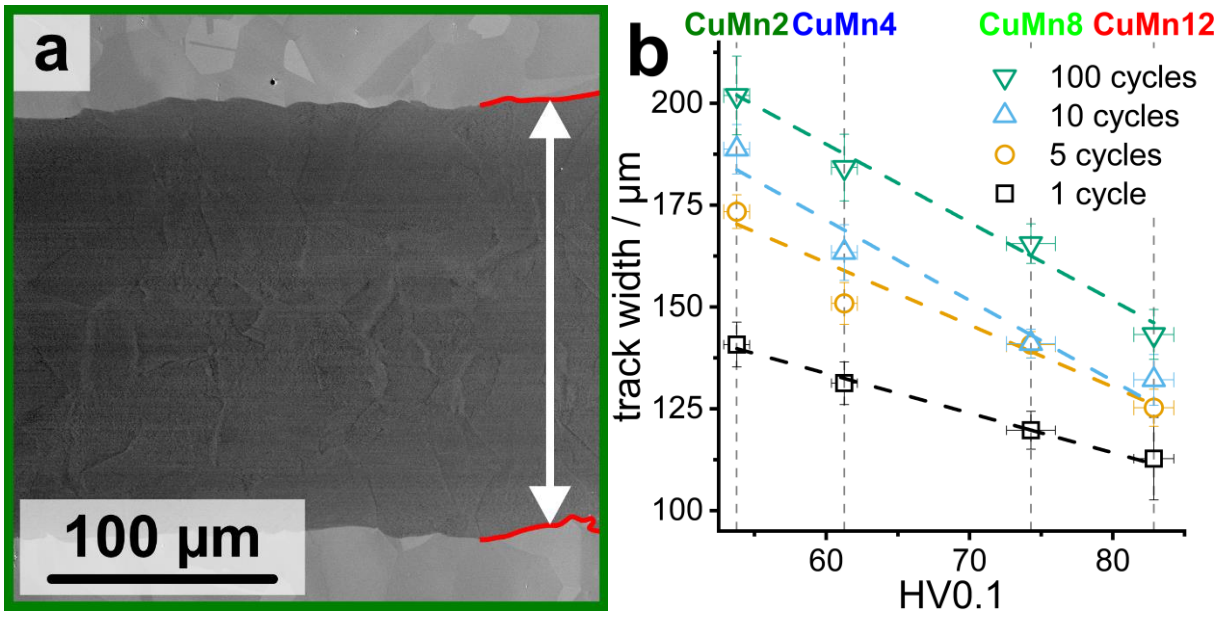

Fig. 4: (a) Top view SEM micrograph (SE contrast) of a wear track on a CuMn2 sample after ten cycles. The sliding direction (SD) is right to left and back again. A small part of the track edge is highlighted with red lines and a white arrow indicates the track width. (b) Determined track width as function of microhardness of the base Cu-Mn alloys in the unloaded state are displayed from one up to 100 cycles. The coefficient of determination $(\mathbf{R^2_{adj}})$ value is above 0.93 for all linear approximations displayed as dotted lines.

3.4. Deformation layer / Cross sections

In order to systematically investigate the influence of dry sliding on the microstructure, FIB cross sections were prepared parallel to the sliding direction (SD) in the center of the wear scar. As depicted in the micrographs in Fig. 5 a & c, already a single sliding pass leads to a well-defined contrast change in the SEM micrograph below the surface. The feature comprises a wavy line with a sharp contrast change in the SEM micrograph on either side. The depth of this feature stays almost constant within a grain, while the depth changes from grain to grain. The observed image contrast in the cross section micrographs is a superposition of SE and BSE signal, as detected by the in-lens detector. This in turn results in an image with topographic information superimposed to atomic contrast and electron channeling information. Therefore, multiple contributions for the formation of the contrast change across the observed feature have to be considered. The freshly generated surface via FIB has no unusual features in its complexion and topographic contrast [41]. Consequently, a topography contribution by the SE signal can be ruled out for the observed feature. Based on similar, previous studies [13,54] and examination of the counter body (not shown here), no mechanical mixing occurs between the surface layer and the sapphire sphere. Hence, chemical BSE contrast is also unlikely to be present. Finally, there is a remaining electron channeling contrast suggestive of a partial crystal rotation at the horizontal line below the surface. To further investigate the nature of this feature TEM foils were prepared near the cross sections by a FIB lift-out technique. In both examined cases, CuMn2 and CuMn12 after a single trace, bright field imaging reveals two distinct horizontal line-like features which are (50 – 70) nm separated from each other (see Fig. 5 b & d). The region between the surface and the outermost horizontal feature in the CuMn2 sample exhibits a uniformly darker contrast as compared to the bulk material below which indicates a lattice rotation of the upper part. As depicted in Fig. 5d, the region above the first and second features appears ‘fragmented’ - indicative of a localized lattice distortion, correlated to the higher solute concentration.

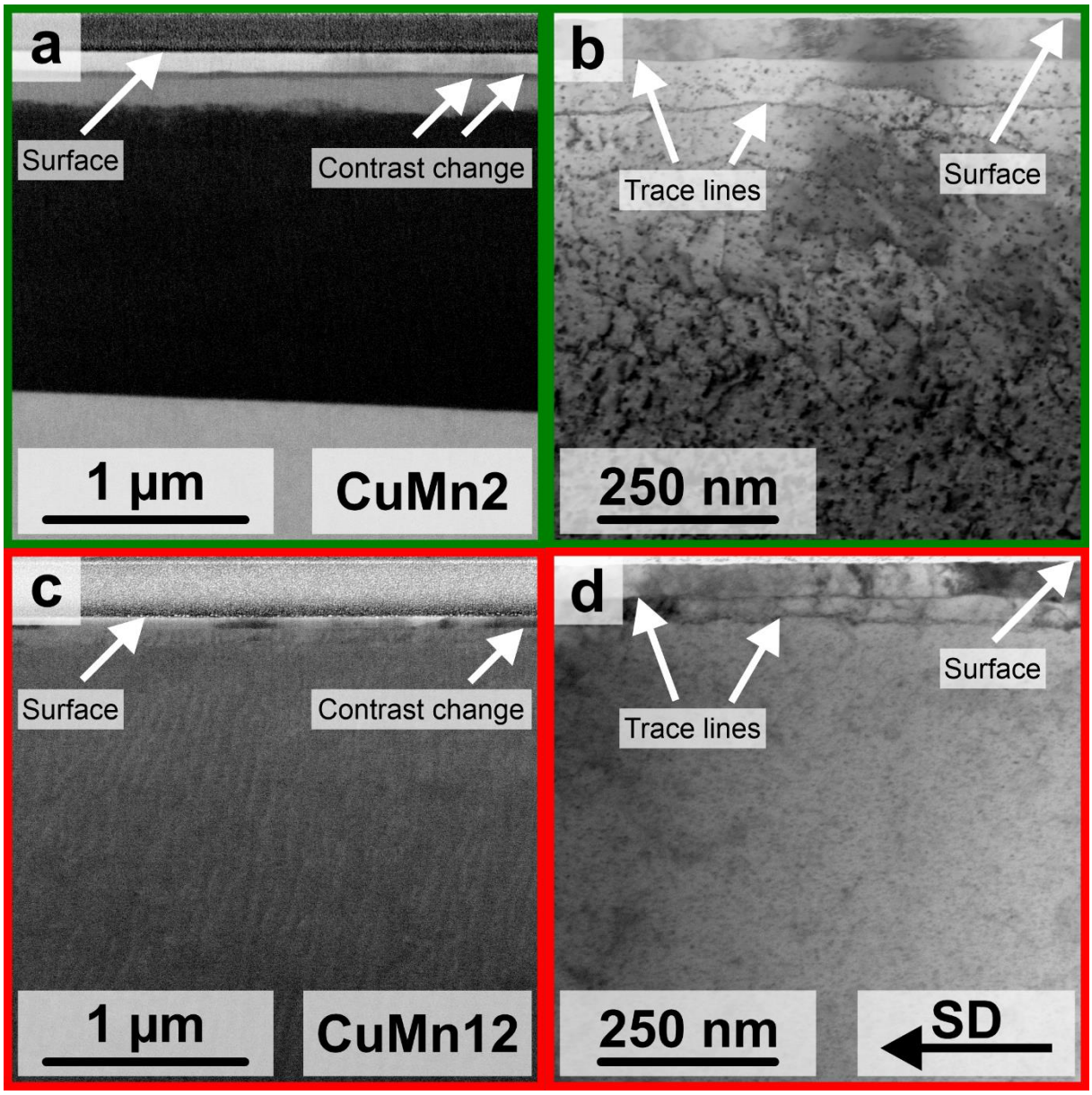

Fig. 5: Overview of the FIB-prepared cross sections and STEM foils; (a) and (c) are SEM micrographs of a cross section of CuMn2 and CuMn12, respectively, after a single trace taken from the center of the track. About 100 nm beneath the surface (note that the cross sectional surface is tilted by 52° with respect to the electron beam), a sharp contrast change is marked. (b) and (d) display bright field STEM micrographs (acquired at 30 kV acceleration voltage) of the same wear tracks as displayed in (a) and (c). In both micrographs, two trace lines are highlighted. In the upper part of the images, Pt protection layers are observed and the sliding direction (SD) is the same in all displayed micrographs.

Small lattice rotations can be mediated by dislocation configurations that develop by the movement and interaction of dislocations upon the deformation during the sliding. This is supported by literature of dry and lubricated high cycle sliding, in which grain shearing and refinement is typically observed [9,10,16,18,20,21,39,54]. The line-like feature observed in the cross sections and the bright field STEM investigations is similar to the dislocation structure recently described by Greiner et al. [39,54]. After a single, dry sliding pass of a sapphire sphere against a flat Cu sample, the authors of the aforementioned publications revealed a distinct microstructural discontinuity in the microstructure at about (100 – 200) nm beneath the surface

which is associated with a lattice rotation of approximately 8° as confirmed by electron transmission techniques. Due to the striking similarity of these observations to the present ones, the feature observed in the transmission micrographs is referred to as dislocation trace line (DTL), or trace line. The overall characteristics of the STEM and SEM cross section micrographs appear similar in all cases. The features observed in the cross sectional images will thus be analyzed in the same way as previously stated, according to Ref. [39,54]. The dislocation trace line is observed independent of solute concentration and grain orientation in all alloys; this indicates that it is an inherent feature of tribologically loaded microstructures in FCC metals and alloys. Furthermore, the depth of the DTL is almost independent of the alloy composition but slightly affected by the grain orientation as visualized by the standard deviations (see Fig. 6a). For example, the uppermost DTL for (0.5 – 5) cycles is observed at a depth of (78 $\pm$ 14) nm. In some of the grains a second DTL was detected (see Fig. 5 a – d and Fig. 6a). However, the origins of the second DTL are still not fully understood.

After five to ten cycles, fine grains (grain size of about (100 – 1000) nm) are observed above the uppermost dislocation trace line. In case of CuMn12, the formation of fine grains can be detected at about five cycles and the dislocation trace line cannot be distinguished from the surrounding dislocation structures beyond that cycle number. After 100 and more cycles, the subsurface microstructure consists of in sliding direction elongated subgrains (aspect ratio greater than 2) and their size increases gradually with increasing depth as depicted in Fig. 6b (see Fig. S4 for cross sections of 10 and 1000 cycles). In coarse-grained metals under significant shear stress, grain refinement is observed due to the dislocation motion as well as due to the collective rearrangement of dislocations in low-angle grain boundaries and later conversion to high angle-grain boundaries [16–18,55]. In the wear traces with 100 or more cycles, a significant amount of oxygen was detected through EDS. However, considering the principle of acquisition and estimation, the presence of oxygen is qualitatively acceptable, however a precise estimation cannot be made. Additionally, small granular structures could be distinguished on the surface of the wear track in the cross sections (right below the protective Pt-layer, see Fig. 6b) and their size and quantity increases with cycle number. This is indicative of spatially separated oxides forming inside the wear track, leading to an overall increase of detected oxygen by EDS as well as the observation of the granular structures. A similar oxidation behavior is reported in literature for coarse-grained Cu and Cu alloys in atmospheric conditions [12,13,17]. Based on these observations, the microstructural evolution is summarized as follows: (i) Initially, there is the formation of at least one DTL after a single sliding pass in all investigated alloys. (ii) After five to ten cycles, the formation of fine grains

is noticed. (iii) In sliding direction, elongated grains and oxide cluster at the surface are observed for 100 and more cycles.

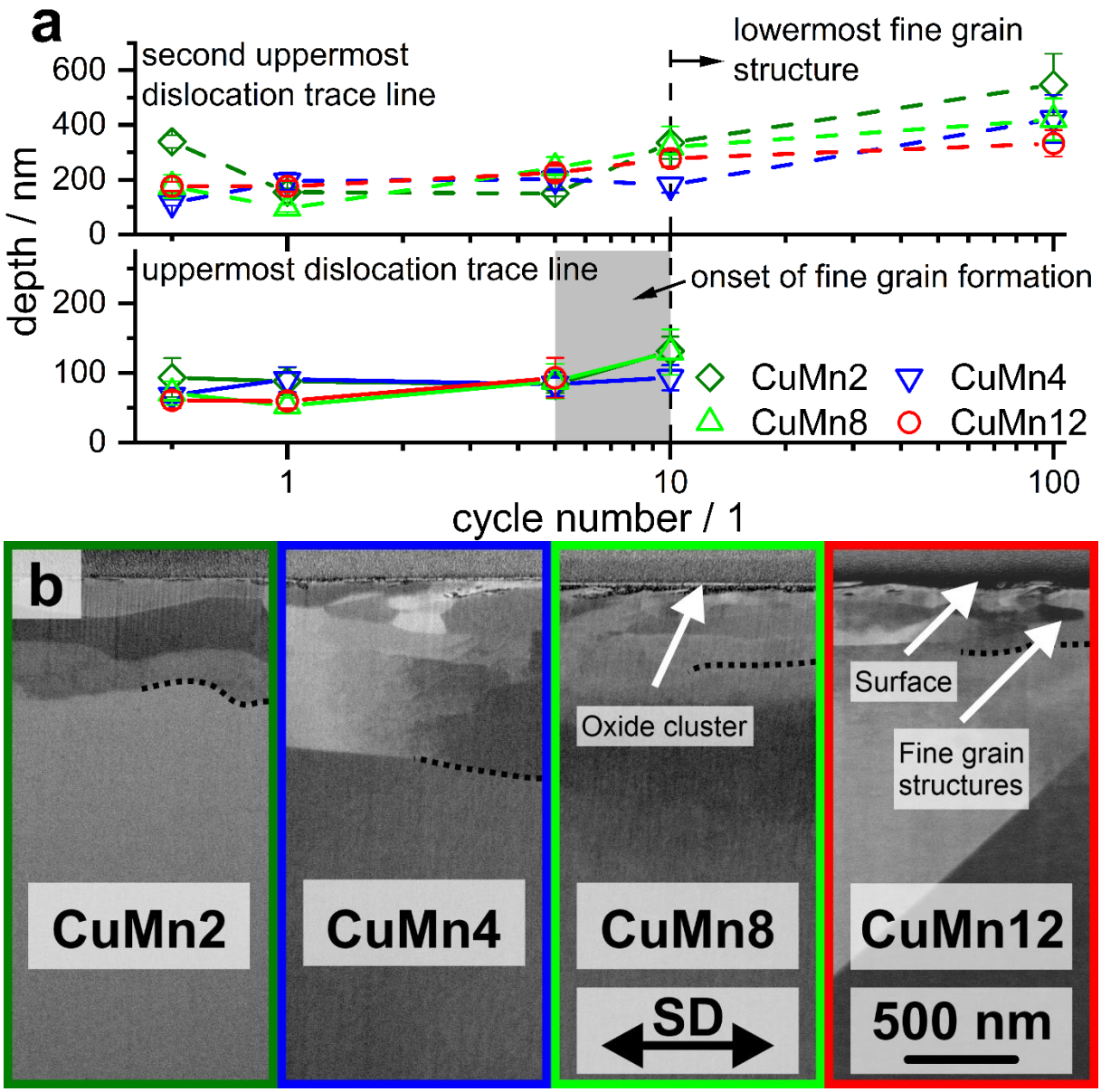

Fig. 6: Compilation of the determined depths of the dislocation traces line and overview of the FIB-prepared cross sections; (a) Determined depth of the uppermost and second uppermost dislocation trace line as well as the lowermost fine grain structure are shown as a function of cycle number. Note that a second dislocation trace line is not found in every grain and the least sharp contrast change is considered for the depth of the lowermost fine grain structure, as highlighted by black dashed lines in (b). The solid and dashed lines in the figure are guides to the eyes. (b) Multiple SEM micrographs of representative cross sections in CuMn2, CuMn4, CuMn8 and CuMn12 (from left to right) after 100 cycles. The lowermost fine grain structures are partly highlighted by black dashed lines. Oxide cluster form at the surface in all alloys.

The interaction between the stress field from dislocations and the strongly inhomogeneous stress field underneath the spherical sliding contact has to be considered in order to rationalize the observed results. The calculation of the subsurface stress field is performed by utilizing the elastic solution from Hamilton and Goodman [57]. The elastic model is not a fully appropriate candidate because of the plastic deformation of the surface. However, it is a reasonable,

analytical model to describe the stress field in a tribological contact [54]. For the calculation, a coefficient of friction of 0.25 is assumed and a normal force of 2 N is used. The experimental coefficient of friction for the first sliding pass cannot be determined exactly, but the friction data supports a value between 0.2 and 0.4. The contact area between the sample and the sapphire sphere is not based on the elastic solution given by Hertz [58] but rather on the determined track widths after one cycle (as depicted in Fig. 4b). Wille and Schwink [56] determined the critical shear stress (CRSS) for the activation of the primary slip system of various Cu-Mn single crystals at RT. They reported an increase of the CRSS from 13 MPa to 25 MPa for CuMn2 to CuMn7.6 (at%), respectively. For the calculations, a rough estimate of the critical shear stress for CuMn8 and CuMn12 is obtained by linear interpolation, based on the data from Ref. [56]. The contour plot on a plane through the center of contact with the counter body is displayed in Fig. 7a. Under the given conditions, the region of maximum shear stress is below the contact surface. At the trailing edge of the spherical counter body, the shear stress τ_{xz} features a sign change from compression to tension. For the sake of simplicity, only a single slip system which is perpendicular to the surface is considered. Therefore, the in-plane shear stress component τ_{xz} can be considered as the major contribution to the force acting on edge dislocations beneath the surface to a first approximation [54]. Based on the sign of the τ_{xz} stress field, the edge part of dislocations is able to glide away from or to the sample surface. These edge dislocations are glissile until reaching the point at which the shear stress is below the critical value. At this point, the edge dislocations will stop moving. Therefore, the shape and magnitude of the stress field at the trailing edge is considered to determine the depth of the DTL [54,59]. Taking into account only the different critical shear stresses of the alloys, the edge part of the dislocations should occur deeper below the surface for higher Mn concentrations. However, an increase in Mn solute concentration leads to a narrower wear track which results in higher absolute stresses in the near-surface region, as depicted in Fig. 7 b & c.

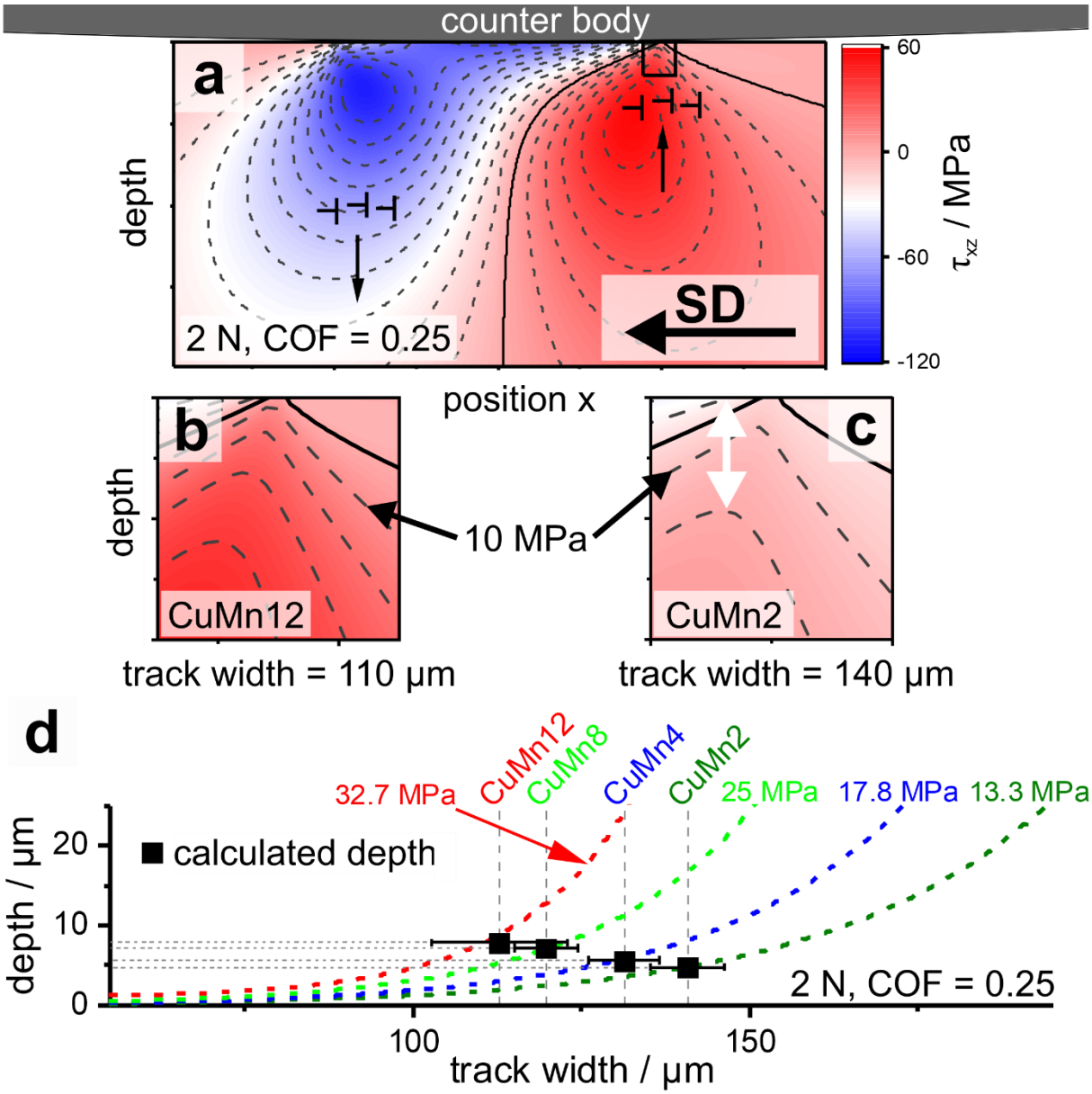

Fig. 7: Stress field based on the Hamilton and Goodman elastic model; (a) The calculated τ_{xz} stress field in the center of the wear scar. The arrow on top indicates the sliding direction (SD). Some (edge) dislocations and their direction of movement are displayed. (b) and (c) are close ups as highlighted in (a) for a track width of 110 µm (CuMn12) and 140 µm (CuMn2), respectively. A white arrow indicates the determined depth in (c). A normal force of 2 N and a COF of 0.25 is used for all calculations. Solid and dotted lines are iso-stress contours. (d) The depth of different contours as a function of track width. Squares indicate the calculated depth of the DTL based on the different critical shear stresses and determined track widths.

Based on the determined track widths and critical shear stresses, the estimated depth of the DTL for each alloy was calculated. As depicted in Fig. 7d, the trend of the depth of the iso-stress contours exhibits a strong correlation with the track width. The calculated depth for the individual compositions is in the range of 5 to 8 µm. Two aspects of the results are noteworthy: (i) The calculated depth is at least one order of magnitude higher than the experimentally determined depths. Besides the limitations of the model mentioned before, the depth is significantly dependent on the track width. So even small changes in the contact area alters the stress field severely. (ii) The evaluated depth of the DTL for the different alloys stays within

the same range, notwithstanding the limitations discussed before. Based on the current results, the fundamental depth of the DTL is influenced by the interrelating and almost opposing contributions of the stress distribution and the critical stress for dislocation motion. Whether different slip modes (wavy and planar slip) have an impact on the depth of the dislocation trace line remains an open question.

4. Conclusion

Cu-Mn alloys with 2 to 12 at% Mn, featuring a constant stacking fault energy, were manufactured to exhibit an equivalent grain size and a surface free of deformation. To investigate the dry sliding tribological behavior against a sapphire sphere under mild load, the cycle number was increased in a systematic fashion from a single pass, up to 100 cycles. Subsequently, the wear track as well as the microstructure beneath the surface was scrutinized. Under mild tribological load, the width of the wear track exhibits a linear correlation with the bulk microhardness until 100 cycles. The increasing hardness within the Cu-Mn alloys with increasing solute content is quantitatively described by means of the Labusch model for solid solution strengthening. After just one pass of the sapphire sphere over the flat sample, a distinct change in contrast could be observed in the near-surface region by SEM. For the investigated alloy compositions, the depth of the horizontal dislocation feature appears to be almost independent of the Mn content. The application of an elastic stress field model indicates that the depth of the dislocation feature correlates with the stress distribution as well as the critical stress for dislocation motion. The subsurface microstructure features a transition from the dislocation trace line to subgrains after about five to ten cycles. With increasing deformation of the surface, oxide clusters are formed on the sliding surface and the grains elongate in the direction of sliding.

Declaration of interests

The authors declare that they have no known competing financial interests or personal relationships that could have appeared to influence the work reported in this paper.

Acknowledgments

This work was partially funded by the European Research Council (ERC) under Grant No. 771237, TriboKey. The authors acknowledge the chemical analysis by ICP-OES at the Institute for Applied Materials (IAM-AWP), Karlsruhe Institute of Technology (KIT). Furthermore, we would like to express our gratitude to D. Seifert (Leibniz IFW Dresden) for performing the cold work by rolling. We also thank A. Dollmann, C. Haug and J. Lehmann for

experimental support with the tribological setup as well as A. Srinivasan Tirunilai and B.-D. Nguyen for support with the manuscript.

5. References

[1] W.G. Sawyer, N. Argibay, D.L. Burris, B.A. Krick, Mechanistic Studies in Friction and Wear of Bulk Materials, Annual Review of Materials Research 44 (2014) 395–427. https://doi.org/10.1146/annurev-matsci-070813-113533.

[2] T.D.B. Jacobs, C. Greiner, K.J. Wahl, R.W. Carpick, Insights into tribology from in situ nanoscale experiments, MRS Bulletin 44 (2019) 478–486. https://doi.org/10.1557/mrs.2019.122.

[3] X. Chen, R. Schneider, P. Gumbsch, C. Greiner, Microstructure evolution and deformation mechanisms during high rate and cryogenic sliding of copper, Acta Materialia 161 (2018) 138–149. https://doi.org/10.1016/j.actamat.2018.09.016.

[4] S.C. Lim, Recent developments in wear-mechanism maps, Tribology International 31 (1998) 87–97. https://doi.org/10.1016/S0301-679X(98)00011-5.

[5] S.C. Lim, M.F. Ashby, Overview no. 55 Wear-Mechanism maps, Acta Metallurgica 35 (1987) 1–24. https://doi.org/10.1016/0001-6160(87)90209-4.

[6] P.J. Blau, Fifty years of research on the wear of metals, Tribology International 30 (1997) 321–331. https://doi.org/10.1016/S0301-679X(96)00062-X.

[7] D.A. Rigney, Sliding Wear of Metals, Annual Review of Materials Science 18 (1988) 141–163. https://doi.org/10.1146/annurev.ms.18.080188.001041.

[8] F.P. Bowden, D. Tabor, The friction and lubrication of solids, Oxford University Press, Oxford, 2008.

[9] D.A. Rigney, W.A. Glaeser, The significance of near surface microstructure in the wear process, Wear 46 (1978) 241–250. https://doi.org/10.1016/0043-1648(78)90125-4.

[10] D.A. Rigney, J.P. Hirth, Plastic deformation and sliding friction of metals, Wear 53 (1979) 345–370. https://doi.org/10.1016/0043-1648(79)90087-5.

[11] N.P. Suh, The delamination theory of wear, Wear 25 (1973) 111–124. https://doi.org/10.1016/0043-1648(73)90125-7.

[12] X. Chen, Z. Han, K. Lu, Wear mechanism transition dominated by subsurface recrystallization structure in Cu–Al alloys, Wear 320 (2014) 41–50. https://doi.org/10.1016/j.wear.2014.08.010.

[13] Z. Liu, C. Patzig, S. Selle, T. Höche, P. Gumbsch, C. Greiner, Stages in the tribologically-induced oxidation of high-purity copper, Scripta Materialia 153 (2018) 114–117. https://doi.org/10.1016/j.scriptamat.2018.05.008.

[14] T.J. Rupert, C.A. Schuh, Sliding wear of nanocrystalline Ni–W: Structural evolution and the apparent breakdown of Archard scaling, Acta Materialia 58 (2010) 4137–4148. https://doi.org/10.1016/j.actamat.2010.04.005.

[15] X. Chen, Z. Han, K. Lu, Friction and Wear Reduction in Copper with a Gradient Nano-grained Surface Layer, ACS Applied Materials & Interfaces 10 (2018) 13829–13838. https://doi.org/10.1021/acsami.8b01205.

[16] D.A. Hughes, N. Hansen, Graded Nanostructures Produced by Sliding and Exhibiting Universal Behavior, Phys. Rev. Lett. 87 (2001) 135503. https://doi.org/10.1103/PhysRevLett.87.135503.

[17] S.V. Prasad, J.R. Michael, T.R. Christenson, EBSD studies on wear-induced subsurface regions in LIGA nickel, Scripta Materialia 48 (2003) 255–260. https://doi.org/10.1016/S1359-6462(02)00376-7.

[18] A. Emge, S. Karthikeyan, D.A. Rigney, The effects of sliding velocity and sliding time on nanocrystalline tribolayer development and properties in copper, Wear 267 (2009) 562–567. https://doi.org/10.1016/j.wear.2008.12.102.

[19] A. Singh, M. Dao, L. Lu, S. Suresh, Deformation, structural changes and damage evolution in nanotwinned copper under repeated frictional contact sliding, Acta Materialia 59 (2011) 7311–7324. https://doi.org/10.1016/j.actamat.2011.08.014.

[20] K. Wolff, Z. Liu, D. Braun, J. Schneider, C. Greiner, Chronology of the microstructure evolution for pearlitic steel under unidirectional tribological loading, Tribology International 102 (2016) 540–545. https://doi.org/10.1016/j.triboint.2016.06.016.

[21] N. Argibay, M. Chandross, S. Cheng, J.R. Michael, Linking microstructural evolution and macro-scale friction behavior in metals, Journal of Materials Science 52 (2017) 2780–2799. https://doi.org/10.1007/s10853-016-0569-1.

[22] J.J. Wert, S.A. Singerman, S.G. Caldwell, D.K. Chaudhuri, An x-ray diffraction study of the effect of stacking fault energy on the wear behavior of Cu-Al alloys, Wear 92 (1983) 213–229. https://doi.org/10.1016/0043-1648(83)90196-5.

[23] J.J. Wert, S.A. Singerman, S.G. Caldwell, R.A. Quarles, The role of stacking fault energy and induced residual stresses on the sliding wear of aluminum bronze, Wear 91 (1983) 253–267. https://doi.org/10.1016/0043-1648(83)90071-6.

[24] J.J. Wert, W.M. Cook, The influence of stacking fault energy and adhesion on the wear of copper and aluminum bronze, Wear 123 (1988) 171–192. https://doi.org/10.1016/0043-1648(88)90098-1.

[25] P.J. Blau, A Study of the interrelationships among wear, friction and microstrucutre in the unlubricated sliding of copper and several single-phase binary copper alloys. Dissertation, 1979.

[26] N.P. Suh, N. Saka, The stacking fault energy and delamination wear of single-phase f.c.c. metals, Wear 44 (1977) 135–143. https://doi.org/10.1016/0043-1648(77)90091-6.

[27] J.W. Christian, S. Mahajan, Deformation twinning, Progress in Materials Science 39 (1995) 1–157. https://doi.org/10.1016/0079-6425(94)00007-7.

[28] Z. Wang, Cyclic deformation response of planar-slip materials and a new criterion for the wavy-to-planar-slip transition, Philosophical Magazine 84 (2004) 351–379. https://doi.org/10.1080/14786430310001639824.

[29] V. Gerold, H.P. Karnthaler, On the origin of planar slip in f.c.c. alloys, Acta Metallurgica 37 (1989) 2177–2183. https://doi.org/10.1016/0001-6160(89)90143-0.

[30] K. Wolf, H.-J. Gudladt, H.A. Calderon, G. Kostorz, Transition between planar and wavy slip in cyclically deformed short-range ordered alloys, Acta Metallurgica et Materialia 42 (1994) 3759–3765. https://doi.org/10.1016/0956-7151(94)90441-3.

[31] S.I. Hong, C. Laird, Mechanisms of slip mode modification in F.C.C. solid solutions, Acta Metallurgica et Materialia 38 (1990) 1581–1594. https://doi.org/10.1016/0956-7151(90)90126-2.

[32] S.I. Hong, Criteria for predicting twin-induced plasticity in solid solution copper alloys, Materials Science and Engineering: A 711 (2018) 492–497. https://doi.org/10.1016/j.msea.2017.11.076.

[33] K. Nakajima, K. Numakura, Effect of solute atoms on stacking faults Cu-Ni and Cu-Mn systems, Philosophical Magazine 12 (1964) 361–368. https://doi.org/10.1080/14786436508218878.

[34] T. Steffens, C. Schwink, A. Korner, H.P. Karnthaler, Transmission electron microscopy study of the stacking-fault energy and dislocation structure in CuMn alloys, Philosophical Magazine A 56 (1987) 161–173. https://doi.org/10.1080/01418618708205159.

[35] P.C.J. Gallagher, The influence of alloying, temperature, and related effects on the stacking fault energy, Metallurgical Transactions 1 (1970) 2429–2461. https://doi.org/10.1007/BF03038370.

[36] C.B. Carter, I.L.F. Ray, On the stacking-fault energies of copper alloys, The Philosophical Magazine: A Journal of Theoretical Experimental and Applied Physics 35 (1977) 189–200. https://doi.org/10.1080/14786437708235982.

[37] A. Howie, P.R. Swann, Direct measurements of stacking-fault energies from observations of dislocation nodes, The Philosophical Magazine: A Journal of Theoretical Experimental and Applied Physics 6 (1961) 1215–1226. https://doi.org/10.1080/14786436108243372.

[38] J.B. Nelson, D.P. Riley, An experimental investigation of extrapolation methods in the derivation of accurate unit-cell dimensions of crystals, Proceedings of the Physical Society 57 (1945) 160. https://doi.org/10.1088/0959-5309/57/3/302.

[39] C. Greiner, Z. Liu, L. Strassberger, P. Gumbsch, Sequence of Stages in the Microstructure Evolution in Copper under Mild Reciprocating Tribological Loading, ACS Applied Materials & Interfaces 8 (2016) 15809–15819. https://doi.org/10.1021/acsami.6b04035.

[40] A. Wanner, Elastic modulus measurements of extremely porous ceramic materials by ultrasonic phase spectroscopy, Materials Science and Engineering: A 248 (1998) 35–43. https://doi.org/10.1016/S0921-5093(98)00524-3.

[41] J. Mayer, L.A. Giannuzzi, T. Kamino, J. Michael, TEM Sample Preparation and FIB-Induced Damage, MRS Bulletin 32 (2007) 400–407. https://doi.org/10.1557/mrs2007.63.

[42] N.A. Gokcen, The Cu-Mn (copper-manganese) system, Journal of Phase Equilibria 14 (1993) 76–83. https://doi.org/10.1007/BF02652163.

[43] R.W. Olesinski, G.J. Abbaschian, The Cu−Ge (Copper-Germanium) system, Bulletin of Alloy Phase Diagrams 7 (1986) 28–35. https://doi.org/10.1007/BF02874979.

[44] L. Vegard, Die Konstitution der Mischkristalle und die Raumfüllung der Atome, Zeitschrift für Physik 5 (1921) 17–26. https://doi.org/10.1007/BF01349680.

[45] R. Labusch, A Statistical Theory of Solid Solution Hardening, physica status solidi (b) 41 (1970) 659–669. https://doi.org/10.1002/pssb.19700410221.

[46] K.L. Johnson, Contact Mechanics, 9th ed., Cambridge University Press, Cambridge, 2003.

[47] T.H. Wille, W. Gieseke, C.H. Schwink, Quantitative analysis of solution hardening in selected copper alloys, Acta Metallurgica 35 (1987) 2679–2693. https://doi.org/10.1016/0001-6160(87)90267-7.

[48] M.Z. Butt, On the deviation from random distribution of solute atoms in some copper-based alloys, Solid State Communications 72 (1989) 139–141. https://doi.org/10.1016/0038-1098(89)90894-6.

[49] E.M. Sokolovskaya, A.T. Grigorev, E.M. Smimova, Transformations in the Solid State of Copper-Manganese Alloys, Zhurnal Neorganicheskoi Khimii (1962) 2636–2638.

[50] W.L. Li, N.R. Tao, Z. Han, K. Lu, Comparisons of dry sliding tribological behaviors between coarse-grained and nanocrystalline copper, Wear 274-275 (2012) 306–312. https://doi.org/10.1016/j.wear.2011.09.010.

[51] K. Kato, Classification of wear mechanisms/models, Proceedings of the Institution of Mechanical Engineers, Part J: Journal of Engineering Tribology 216 (2002) 349–355. https://doi.org/10.1243/135065002762355280.

[52] K. Kato, Abrasive wear of metals, Tribology International 30 (1997) 333–338. https://doi.org/10.1016/S0301-679X(96)00063-1.

[53] J.P. Hirth, D.A. Rigney, Crystal plasticity and the delamination theory of wear, Wear 39 (1976) 133–141. https://doi.org/10.1016/0043-1648(76)90229-5.

[54] C. Greiner, Z. Liu, R. Schneider, L. Pastewka, P. Gumbsch, The origin of surface microstructure evolution in sliding friction, Scripta Materialia 153 (2018) 63–67. https://doi.org/10.1016/j.scriptamat.2018.04.048.

[55] R. Sedláček, W. Blum, J. Kratochvíl, S. Forest, Subgrain formation during deformation: Physical origin and consequences, Metallurgical and Materials Transactions A 33 (2002) 319–327. https://doi.org/10.1007/s11661-002-0093-6.

[56] T.H. Wille, CH. Schwink, Precision measurements of critical resolved shear stress in CuMn alloys, Acta Metallurgica 34 (1986) 1059–1069. https://doi.org/10.1016/0001-6160(86)90216-6.

[57] G.M. Hamilton, L.E. Goodman, The Stress Field Created by a Circular Sliding Contact, J. Appl. Mech. 33 (1966) 371. https://doi.org/10.1115/1.3625051.

[58] H. Hertz, Ueber die Berührung fester elastischer Körper, Journal für die reine und angewandte Mathematik (1881) 156–171.

[59] C. Greiner, J. Gagel, P. Gumbsch, Solids Under Extreme Shear: Friction-Mediated Subsurface Structural Transformations, Advanced Materials 31 (2019). https://doi.org/10.1002/adma.201806705.